MJO Signals in Latent Heating: Results from TRMM Retrievals

CHIDONG ZHANG,* JIAN LING,* SAMSON HAGOS,*,+ WEI-KUO TAO,# STEVE LANG,# YUKARI N. TAKAYABU,@ SHOICHI SHIGE,& MASAKI KATSUMATA,** WILLIAM S. OLSON,++ AND TRISTAN L'ECUYER##

* *RSMAS, University of Miami, Miami, Florida*
\# *GSFC, NASA, Greenbelt, Maryland*
@ *Center for Climate System Research, University of Tokyo, Tokyo, Japan*
& *Graduate School of Science, Kyoto University, Kyoto, Japan*
** *RIGC, Japan Agency for Marine-Earth Science and Technology, Yokosuka, Japan*
++ *JCET, University of Maryland, Baltimore County, Baltimore, Maryland*
Department of Atmospheric Science, Colorado State University, Fort Collins, Colorado

(Manuscript received 4 December 2009, in final form 9 June 2010)

ABSTRACT

Four Tropical Rainfall Measuring Mission (TRMM) datasets of latent heating were diagnosed for signals in the Madden–Julian oscillation (MJO). In all four datasets, vertical structures of latent heating are dominated by two components—one deep with its peak above the melting level and one shallow with its peak below. Profiles of the two components are nearly ubiquitous in longitude, allowing a separation of the vertical and zonal/temporal variations when the latitudinal dependence is not considered. All four datasets exhibit robust MJO spectral signals in the deep component as eastward propagating spectral peaks centered at a period of 50 days and zonal wavenumber 1, well distinguished from lower- and higher-frequency power and much stronger than the corresponding westward power. The shallow component shows similar but slightly less robust MJO spectral peaks. MJO signals were further extracted from a combination of bandpass (30–90 day) filtered deep and shallow components. Largest amplitudes of both deep and shallow components of the MJO are confined to the Indian and western Pacific Oceans. There is a local minimum in the deep components over the Maritime Continent. The shallow components of the MJO differ substantially among the four TRMM datasets in their detailed zonal distributions in the Eastern Hemisphere. In composites of the heating evolution through the life cycle of the MJO, the shallow components lead the deep ones in some datasets and at certain longitudes. In many respects, the four TRMM datasets agree well in their deep components, but not in their shallow components and in the phase relations between the deep and shallow components. These results indicate that caution must be exercised in applications of these latent heating data.

1. Introduction

The Madden–Julian oscillation (MJO; Madden and Julian 1971, 1972) is commonly viewed as driven by convection–circulation coupling or interaction. Such a perception comes mainly from observed coherence between winds and convective signals, such as outgoing longwave radiation (OLR) and precipitation [see Madden and Julian (1994), Lau and Waliser (2005), and Zhang (2005) for summaries of MJO observations]. This perception has been a basis for the development of simple models for understanding certain aspects of MJO dynamics. It has often been assumed, explicitly or otherwise, that diabatic heating associated with the MJO takes a simple profile with its peak in the midtroposphere and becomes zero at the surface and tropopause. The corresponding atmospheric circulation is of the first baroclinic structure, with winds of the opposite directions in the lower and upper troposphere. Under this assumption, the atmosphere is often treated as a single level (or layer) in the study of the MJO [see summaries of theoretical studies on the MJO by Wang (2005), Zhang (2005), and Raymond and Fuchs (2009)].

+ Current affiliation: Pacific Northwest National Laboratory, Richland, Washington.

Corresponding author address: Chidong Zhang, RSMAS/MPO, University of Miami, 4600 Rickenbacker Causeway, Miami, FL 33149.
E-mail: czhang@rsmas.miami.edu

DOI: 10.1175/2010JAS3398.1

This simple conventional approach of representing the diabatic heating profile of the MJO has, however, been challenged. Since the very early stage of MJO research, efforts have been made to explain the slow eastward propagating speed ($\sim$5 m s^{-1}) of the MJO in observations in contrast to the unrealistically fast speeds of intraseasonal oscillations in numerical simulations by simple as well as complex numerical models. For example, Chang (1977) showed that the phase speed of the equatorial Kelvin wave is reduced when friction is explicitly included in the linear wave theory (Matsuno 1966). According to such linear theory of the equatorial waves, the phase speed c of the Kelvin wave is directly related to the equivalent depth h as $c = (gh)^{1/2}$. It was pointed out that if tropical diabatic heating, mainly convective latent heating, had its peak in the lower troposphere, rather than the mid- or upper troposphere, the vertical scales of the perturbations, measured by the equivalent depth, would be reduced, and so would the phase speed of the MJO (Chang and Lim 1988; Sui and Lau 1989). This idea was not further pursued, largely because tropical convective latent heating has long been perceived as dominated by heating related to deep convective and stratiform precipitation from mature mesoscale convective systems with its peak in the upper troposphere (Houze 1997).

The recent development of theoretical understanding of tropical convectively related perturbations has considered the MJO a ''moisture mode'' (Raymond and Fuchs 2009). Such a moisture mode would become unstable and grow when the gross moist stability (GMS; Neelin and Held 1987) is negative. Low-level mass flux and moisture convergence associated with shallow diabatic heating can effectively yield negative GMS (Sobel 2007; Raymond et al. 2009). It has also been suggested that low-level heating is more efficient in inducing large-scale moisture convergence in the boundary layer and lower troposphere as the main energy supply for the MJO (Wu 2003). These ideas have roused new interest in shallow heating associated with the MJO.

Conditions that lead to negative GMS indeed exist in the tropical region with prominent MJO signals. Field observations during the Tropical Ocean–Global Atmosphere Coupled Ocean–Atmosphere Response Experiment (TOGA COARE, November 1992–February 1993; Webster and Lukas 1992) indicated that, in addition to deep convection, the western Pacific warm pool is full of shallow precipitating convection that would supply the atmosphere with heating in the lower troposphere (e.g., Johnson et al. 1999), resulting in negative GMS (López Carrillo and Raymond 2005). Observations have suggested that shallow precipitating clouds might become more prominent during the transition from convectively inactive to active phases of the MJO (e.g., Kikuchi and Takayabu 2004). This and the trailing stratiform-like upper-level heating west of the convection center yield a westward tilt of diabatic heating profiles associated with the eastward propagating MJO. This has been shown in some observational studies (Lin et al. 2004; Kiladis et al. 2005). Other studies, however, failed to detect without ambiguity this tilt in latent or diabatic heating based on satellite observations, global reanalysis products, and sounding observations (Morita et al. 2006; Jiang et al. 2009; Katsumata et al. 2009).

Modeling studies also produced inconsistent results in this regard. Some numerical simulations that exhibit certain observed features of the MJO produced shallow heating immediately preceding deep heating (Zhang and Mu 2005; Benedict and Randall 2007), whereas others did not (Masunaga et al. 2008; Maloney 2009). In some numerical models, shallow heating appears to play an essential role in MJO simulations (Li et al. 2009; Zhang and Song 2009). In others, top-heavy, stratiform-like heating is critical to reproduction of the MJO (Fu and Wang 2009). Nonetheless, the uncertainties in observations, numerical simulations, and theoretical studies (Khouider and Majda 2006, 2008) have emphasized the importance of the shallow to deep structural evolution of latent heating in the MJO. Further investigations on issues related to the vertical structure and evolution of latent heating are needed to advance our understanding of MJO dynamics. This serves as the main motivation of this study.

MJO signals in latent heating and their structural evolution estimated from satellite observations are explored in this study. A common practice of diagnosing MJO signals is making a composite using an MJO index based on dynamical and thermodynamical variables (e.g., wind and OLR). This method would help demonstrate the vertical structure of latent heating associated with known MJO dynamical and thermodynamical fields (Lin et al. 2004; Morita et al. 2006; Lau and Wu 2010). In this study, we pose an alternative question: What would the vertical structure of latent heating associated with the MJO be without any reference to its dynamical and thermodynamical fields? If latent heating is truly an essential component of the MJO, then its MJO signals should be identifiable independently of other fields. Efforts of seeking coherence between latent heating and other MJO measures (e.g., wind and OLR) are justifiable only if MJO signals in latent heating can be independently detected. If we fail to identify MJO signals in latent heating without the help of other dynamical and thermodynamical variables, we have to ponder why. This would lead to questions regarding the physical meaning of its coherence with other variables and our current perception of its role in the MJO.

Empirical orthogonal function (EOF) analysis is commonly used to define the MJO. This method, however, usually fails to identify without ambiguity MJO signals in precipitation (or OLR) alone without reference to wind. A single EOF mode represents a stationary pattern. Propagating signals are represented by a pair of EOF modes with their phase in quadrature, with their eigenvalues very close to each other but separated from their neighboring modes according to a given criterion (e.g., North et al. 1982). The EOF analysis applied to tropical precipitation (or OLR) often yields a single leading mode well separated from the second mode, which may or may not be separated from the third mode. Such leading EOF modes represent an intraseasonal stationary oscillation in tropical precipitation (or OLR) over land or over warm water, which can be comparable to or stronger than the eastward propagating component that defines the MJO. The zonal propagating MJO signals in precipitation (or OLR) can be better detected by combining either one with a dynamical variable (e.g., zonal wind) in a multivariate EOF analysis (e.g., Wheeler and Hendon 2004) or by using different versions of EOF that filter out the stationary component, such as extended EOF (Weare and Nasstrom 1982), complex EOF (Maloney et al. 2008), or Hilbert singular value decomposition (HSVD; Zhang and Hendon 1997). None of these methods has been applied to latent heating on the global scale. Whether MJO signals in latent heating can be independently and objectively identified has yet to be determined.

In this study, we will present diagnostics of MJO signals in latent heating based on satellite observations of the Tropical Rainfall Measuring Mission (TRMM; Kummerow et al. 2000). We focus on two topics: (i) the vertical structure and its evolution in latent heating associated with the MJO detected independently of other dynamical and thermodynamical fields and (ii) the similarities and discrepancies of the MJO signals in latent heating based on four TRMM retrieval algorithms. Special attention is paid to the evolution of vertical structure of latent heating during the life cycle of the MJO, which may help address the controversial issue of the relative importance of shallow versus deep heating to the MJO discussed earlier. The comparison among four TRMM retrievals will demonstrate the utility and uncertainty of these satellite remote sensing products. Toward the end of this study, we will relax the constraint and use an independent MJO index to construct the latent heating field associated with the MJO.

The reliability of TRMM retrievals of latent heating profiles is a subject under debate. As with all satellite remote sensing products, there are assumptions and simplifications made in the processes of retrieving latent heating profiles. TRMM retrievals offer an alternative source of information of the latent heating field that provides much better coverage in time and space than what is available from field observations, and they are not affected by the notorious cumulus parameterization problems plaguing numerical models that produce global reanalysis data. Most of them, however, are not immune from problems in parameterization of cloud microphysics because (with one exception) they use look-up tables generated by cloud-system-resolving models (CSRMs) validated against field observations. In general, the latent heating retrievals based on TRMM satellite remote sensing data are no less "observational" than global reanalyses. Both are proxies for observations and their fidelity in representing reality must not be taken for granted.

This study has no intention of providing a comprehensive comparison among the TRMM latent heating datasets, which was done by Tao et al. (2006), or between the TRMM data and observations, which was done by Hagos et al. (2010). Our discussions will be limited to the topic of interest: the MJO. We will focus on the vertical and zonal structures of the MJO signals in latent heating and ignore their meridional dependence. Whether and how the vertical structure of latent heating may vary as the MJO migrates seasonally in latitude (Zhang and Dong 2004) or propagates northward during the summer Asian monsoon season (Waliser 2006) should be discussed in separate studies.

Latent heating data derived from four TRMM retrievals are introduced in section 2a. An unconventional method was applied to extract MJO signals in latent heating, which is described in sections 2b–e. Results are presented in section 3 in terms of spectra, variance, and vertical, zonal, and temporal variability. A summary and discussion are given in section 4.

2. Data and method

a. Latent heating

Four latent heating estimates derived from TRMM observations (Table 1) were used in this study: spectral latent heating (SLH), convective–stratiform heating (CSH), precipitation radar heating (PRH), and the trained radiometer algorithm (TRN). These datasets provide different quantities: latent heating (LH), total diabatic heating Q_1, and latent heating equivalence ($Q_1 - Q_R$, where Q_R is radiative heating). The main difference between LH and $Q_1 - Q_R$ is the flux of vertical eddy transport of sensible heat (Yanai et al. 1973), which is small, except at the melting level and near the tropopause (Mapes 2001; Shie et al. 2003). In this study, we did not distinguish LH from $Q_1 - Q_R$. In this sense, all four TRMM datasets provide LH, while two (CSH and TRN)

TABLE 1. TRMM heating data.

Datasets	SLH	CSH	PRH	TRN
Variable	$Q_1 - Q_R$, LH	Q_1, LH	LH	Q_1, $Q_1 - Q_R$ (≈LH)
Temporal resolution	Daily	Daily	Pentadal	Orbital
Horizontal resolution	0.5° × 0.5°	0.5° × 0.5°	2.5° × 2.5°	0.5° × 0.5°
Vertical levels	19	19	41	29
Algorithm input data	PR (2A25): rain type, surface and melting-level rain rates, PTH	PR + TMI (3G68): rain type, surface rain rate, stratiform rain fraction, rain location (land vs ocean), PTH	PR (2A25): rain type, surface rain rate, rainwater profiles, bright brand height	PR (2A25): rain type, surface rain rate, PTH; TMI: radiance
Lookup table	[rain type, PTH, melting-level rain rate] → LH(z)	[rain type, surface rain rate, stratiform rain fraction, rain location, PTH] → LH(z)	—	[TMI radiance] → LH(z)
Main strength	Nonzero heating for anvil rain with zero surface rain	Larger sample sizes than PR-only estimate	Independent of CSRMs	Larger sample sizes than PR-only estimate
Main weakness	Depend on CSRM-generated lookup tables; limited PR sampling	Depend on CSRM-generated lookup tables; zero LH in regions with zero surface rain	Uncertainty in vertical velocity profiles; limited PR sampling; assuming steady-state and vertically 1D	Depend on CSRM-generated lookup tables; no data over land; zero LH in regions with zero surface rain
Known biases	Underestimated heating in upper troposphere	Underestimated (overestimated) heating above (below) 9 km	Underestimated (overestimated) LH above (below) melting level	Overestimated shallow convective heating; accounting of boundary-layer sensible heating
References	Shige et al. (2004, 2007, 2008, 2009)	Tao et al. (1993, 2000, 2010)	Kodama et al. (2009)	Grecu and Olson (2006); Grecu et al. (2009)

provide Q_1. For direct comparisons, we used LH from all four datasets and will make a comment in section 4 on results based on Q_1.

In the SLH algorithm (Shige et al. 2004, 2007, 2008, 2009), a lookup table (LUT) generated by a CSRM includes vertical profiles of latent heating that vary continuously with precipitation top height (PTH) and precipitation rates at the surface for convective and shallow stratiform rain and with the melting-level rain rate for anvil (deep stratiform) rain. TRMM Precipitation Radar (PR) information of the PTH, precipitation rates, and rain types is used to select vertical profiles of latent heating from the LUT.

Data from a new CSH algorithm (Tao et al. 2010) was used in this study, which is an updated version of the previous one (Tao et al. 1993, 2000). Based on PR information of surface rain rates and stratiform rain fraction, it also uses an LUT generated by a CSRM to select vertical profiles of latent heating for convective and stratiform rain over the ocean and land, respectively, and for shallow rain.

The PRH algorithm (Kodama et al. 2009) estimates latent heating from the growth/evaporation of raindrops during their vertical displacement based on the vertical gradient of the precipitating water with respect to the motion of the precipitating particles. Condensation and deposition (evaporation) are regarded as the cause of observed increases (decreases) in precipitation water amount with respect to the direction of the motion of the precipitating particles. This algorithm does not use information from any numerical model.

In the TRN algorithm (Grecu and Olson 2006; Grecu et al. 2009), PR-based latent heating profiles, coincident TRMM Microwave Imager (TMI) brightness temperature observations, and a CSRM-generated LUT are used to assemble a large database, which is queried to find brightness temperatures consistent with TMI-observed values at a given location. Latent heating profiles, among other parameters, in the database associated with the consistent brightness temperatures are composited using a Bayesian method to find their corresponding ''expected values.'' Total diabatic heating was estimated by combining latent heating with an ancillary atmospheric radiative heating climatology derived on an identical vertical and horizontal grid from an approach known as the Hydrologic Cycle and Earth's Radiation Budget (HERB) algorithm (L'Ecuyer and Stephens 2003, 2007). TRN data are available only over the oceans.

A common known problem of PR-based latent heat retrievals is the inherent sensitivity of the PR that can detect only precipitation-sized particles. This leads to an underestimate of the contribution of nonprecipitating shallow clouds, which should have low-level total heating (e.g., Nitta and Esbensen 1974; Johnson and Lin 1997). An LUT sensitively depends on the CSRM that generates it (e.g., Shige et al. 2009).

Table 1 lists major differences in the four algorithms and their known strengths, weaknesses, and biases. A detailed comparison among them and with other TRMM latent heating datasets was made by Tao et al. (2006). Morita et al. (2006) examined statistical structures of latent heating associated with the MJO using an early version of SLH. Jiang et al. (2009) compared TRN and an early version of CSH to two global data assimilation products for MJO events in boreal winter of 1998/99. Lau and Wu (2010) used multiyear data of TRMM, including an early version of CSH latent heating, to examine the evolution of cloud structure and associated latent heating through the life cycle of the MJO over the western Pacific. Hagos et al. (2010) compared the four TRMM datasets to diabatic heating estimated from sounding observations and global reanalysis products in several tropical regions. The present study focuses on statistical signals of the MJO from the four TRMM latent heating datasets and their longitudinal and temporal variability.

All four datasets cover 10 years (1 January 1998–31 December 2007). The daily data of CSH and SLH and orbital data of TRN were made into pentadal time series. All data were interpolated onto common 2.5° × 2.5° grids and 17 height levels (0.5 and 1–16 km). Latitudinal variability was ignored by taking averages over 15°S–15°N. Zonal mean profiles and variability (mean + 1 standard deviation) of the resulting four TRMM heating datasets are obviously different (Fig. 1, left panels). The mean profiles (solid lines) of SLH and CSH show unique double peaks, one above and one below the melting level (~5.5 km). The double-peak structure is subtle in the mean of TRN and hardly discernable in PRH. The mean profiles of the four TRMM latent heating datasets differ more in the lower than the upper troposphere. This is the first sign of potential large uncertainties in retrievals of latent heating due to shallow convection that produces warm rain and low-level heating.

b. Separation of variables

Two general steps were taken to diagnose the data. The first separated the vertical dependence of heating profiles from their zonal and temporal dependence. The second isolated MJO signals in the vertically independent components of the heating field. Each step involved an analysis of EOF or the like that produced two leading modes of its own. To avoid confusion in terminology, these two steps are described in detail.

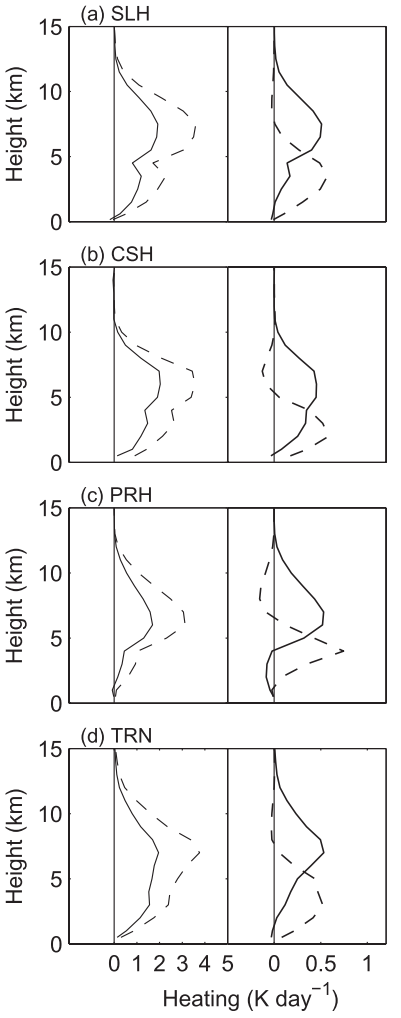

FIG. 1. (left) Zonal means (solid) and means + 1 std dev (dashed). (right) Zonal mean eigenvectors of the first ($\{\mathbf{R}_d\}$, solid) and second ($\{\mathbf{R}_s\}$, dashed) REOF modes.

First, as mentioned earlier, with the latitudinal variability within the tropics ignored for simplicity, a three-dimensional heating field $\mathbf{Q}(x, z, t)$ was generated by averaging over 15°S–15°N, where x is longitude, z is height, and t is time. The latitudinal mean did not completely remove equatorially asymmetric signals such as those in the eastern Pacific, as will be seen later. The time mean $\overline{\mathbf{Q}}(x, z)$ was then removed to create its anomalies $\mathbf{Q}^*(x, z, t)$. At each given longitude x_0, $\mathbf{Q}^*(x_0, z, t)$ was subject to a rotated EOF (REOF) analysis. We used raw VARIMAX REOF in this study. The results cannot be completely reproduced by normal VARIMAX REOF (Kaiser 1958). In normal REOF, heating at each level carries an equal weight in rotation. But heating at the

TABLE 2. Definitions of symbols.

Symbol	Definition
$\overline{Y}$	Time mean of Y
Y^*	Deviation of Y from its time mean
Y'	Intraseasonally filtered Y
$\{Y\}$	Zonal mean of Y
Y_d	First REOF model (deep component) of Y
Y_s	Second REOF model (shallow component) of Y
Y^{MJO}	MJO in Y
$\hat{Y}$	Composite of Y
$A_{\mathbf{H}}$	Amplitude of $\mathbf{H}$
$\mathbf{H}$	Principal components (PCs) of HSVD
Q	Latent heating
$\mathbf{P}$	PCs of REOF
$\mathbf{R}$	Eigenvectors of REOF
$\mathbf{X}$	Eigenvectors of HSVD
σ_Y	Variance of Y

lowest and highest levels is near zero (Fig. 1), which should not be weighted equally as heating at levels with large amplitudes. Raw VARIMAX REOF is thus more appropriate for this study.

With few exceptions, each REOF analysis yielded two leading components. The first is deep, with its peak above the melting level (see details below), denoted $\mathbf{Q}_d(x_0, z, t) = \mathbf{R}_d(x_0, z)\mathbf{P}_d(x_0, t)$, where $\mathbf{R}_d(x_0, z)$ is its eigenvector and $\mathbf{P}_d(x_0, t)$ its time series or principal component (PC). The second component is shallow, with its peak below the melting level, denoted $\mathbf{Q}_s(x_0, z, t) = \mathbf{R}_s(x_0, z)\mathbf{P}_s(x_0, t)$. A list of symbols used in this study is given in Table 2. At all longitudes, total heating can be approximated by these first two leading REOF components:

$$\mathbf{Q}(x,z,t) = \overline{\mathbf{Q}}(x,z) + \mathbf{Q}^*(x,z,t) \approx \overline{\mathbf{Q}}(x,z) + \mathbf{Q}_d(x,z,t) + \mathbf{Q}_s(x,z,t). \quad (1)$$

The approximation of $\mathbf{Q}^*(x, z, t)$ in terms of the first two leading REOF components can be written as $\mathbf{Q}^*(x, z, t) \approx \mathbf{R}(x, z)\mathbf{P}(x, t)$, with $\mathbf{R} = [\mathbf{R}_d(x, z), \mathbf{R}_s(x, z)]$ being their eigenvector matrix and $\mathbf{P} = [\mathbf{P}_d(x, t), \mathbf{P}_s(x, t)]^{\mathrm{T}}$ their PC matrix. The right panels in Fig. 1 show the vertical structures of these two components for the four TRMM datasets. Despite the distinct mean profiles of the four TRMM latent heating datasets (e.g., with or without double peaks), their zonally averaged first REOF components are all deep (with peaks above the melting level) and second modes are all shallow (peaks below the melting level). There are discernable discrepancies in the two leading REOF components of the four latent heat datasets: the amplitude of the deep component is not close to zero in the lower troposphere only in PRH; the deep components exhibit two peaks only in SLH and CSH; the amplitudes of the shallow components are not close to zero above the melting level only in CSH and PRH; and the peak level of the shallow component is the lowest in CSH among the four, possibly due to a unique rain type (warm rain) in its retrieval algorithm, and highest in PRH, possibly because of reduced sampling of low-level heating by its treatment of surface clutter of PR signals. The deep versus shallow structures in the leading REOF components are, however, the same for all four datasets. They exist also in diabatic heating derived from in situ sounding observations and global reanalysis products (Hagos et al. 2010).

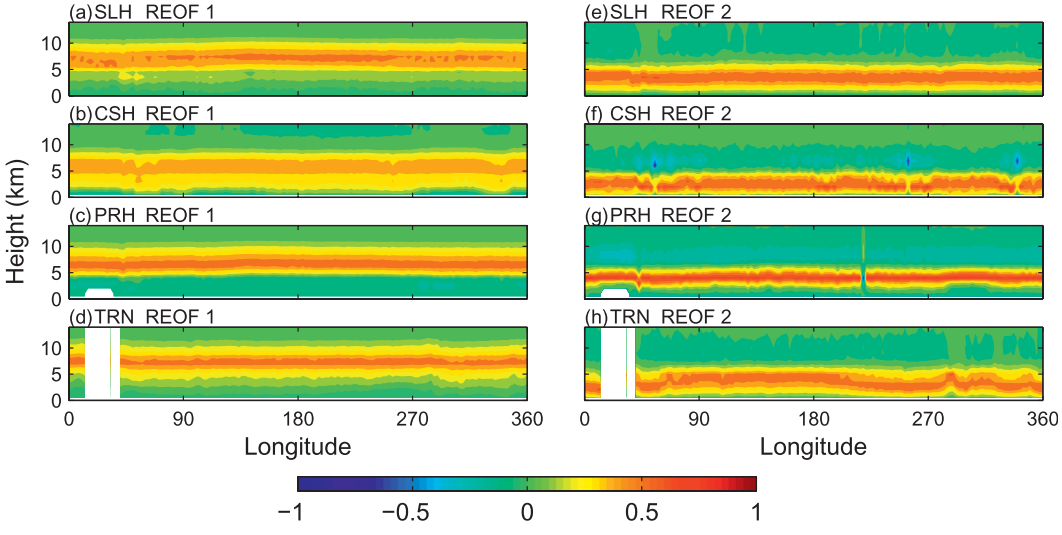

FIG. 2. Eigenvector of $\mathbf{R}_d(x, z)$ (REOF 1, left) and $\mathbf{R}_s(x, z)$ (REOF 2, right).

Another interesting feature of the two leading REOF components is that their vertical structure is nearly ubiquitous in longitude (Fig. 2). There are a few exceptions. The zonal variation of the deep component of CSH is more obvious than the other three. The slightly elevated peak level of the shallow component of TRN over the Maritime Continent might be related to its sampling issues (no data over land). Nevertheless, zonal ubiquity roughly exists for the deep components and, to a lesser degree, the shallow components. The spatial ubiquity of the deep and shallow components also exists in total diabatic heating derived from sounding observations and global reanalysis products (Zhang and Hagos 2009; Hagos et al. 2010). The reason for this ubiquity is unclear, given the large spatial variability in tropical precipitation composition, such as the convective–stratiform rain rate ratio (Schumacher and Houze 2003). It may be related to the two distinct rain formation processes (liquid versus ice) or the two large-scale stability regimes separated by the minimum equivalent potential temperature in the midtroposphere. In any case, this ubiquity leads to a convenient simplification of our diagnostic procedure.

Figure 3 shows that because $\mathbf{R}(x, z)$ does not vary much zonally (i.e., zonal ubiquity), the variance of $\mathbf{R}(x, z)\mathbf{P}(x, t)$ is very close to that of $\{\mathbf{R}\}(z)\mathbf{P}(x, t)$, that is, $\sigma_{\mathrm{RP}} \approx \sigma_{\{\mathrm{R}\}\mathrm{P}}$, where $\{\cdot\}$ represents zonal mean. This validates an approach of replacing $\mathbf{R}(x, z)$ with $\{\mathbf{R}\}(z)$ in representing the heating anomalies, $\mathbf{Q}^*(x, z, t) \approx \{\mathbf{R}\}(z)\mathbf{P}(x, t)$. When the vertical dependence of the three-dimensional field $\mathbf{Q}^*$ is separable from its zonal and temporal dependence this way, the conventional approach of extracting MJO signals from variables at a single level (e.g., precipitation, zonal winds at 850 or 200 hPa) can be directly applied to $\mathbf{P}(x, t)$. We adapted this approach of separation of variables and extracted MJO signals in $\mathbf{Q}^*$ from $\mathbf{P}(x, t)$. The variability in the vertical structure in $\mathbf{Q}^*$ was recovered later by combining the MJO signals in $\mathbf{P}(x, t)$ with the vertical component $\{\mathbf{R}\}(z)$, which will be described next in more detail.

c. MJO identification

To isolate MJO signals, the PC [i.e., $\mathbf{P}(x, t)$] was subjected to an intraseasonal (30–90 day) bandpass filtering, which yielded its intraseasonal anomaly $\mathbf{P}'$. This bandpass filtering is justified by the intraseasonal peaks shown in the time–space spectra (section 3a). We applied an EOF analysis to extract MJO signals from the intraseasonal anomalies of latent heating $\mathbf{P}'$. No pair of EOF modes could, however, be identified for $\mathbf{P}_d$ and $\mathbf{P}_s$ individually, or their combination $\mathbf{P}'$ for any of the four TRMM datasets. Only the first EOF mode is outstanding or separated from the neighboring mode, suggesting that a stationary component in latent heating in $\mathbf{P}_d$, $\mathbf{P}_s$, and $\mathbf{P}'$ dominates any propagating component. The EOF method thus fails to objectively identify and isolate MJO signals in latent heating for the reason discussed in section 1.

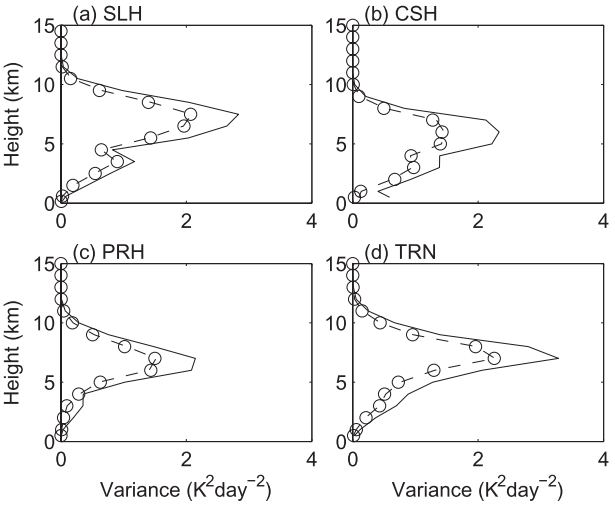

FIG. 3. Zonal and temporal variance of Q (solid line), reconstructed heating using the two leading REOF modes $\mathbf{R}(x, z)\mathbf{P}(x, t)$ ($\sigma_{\mathbf{RP}}$, dashed), and reconstructed heating using the two leading REOF modes with zonally averaged eigenvectors $\{\mathbf{R}\}(z)\mathbf{P}(x, t)$ ($\sigma_{\{\mathbf{R}\}\mathbf{P}}$, circles).

We then applied an HSVD method. It is an SVD analysis of a field and its Hilbert transform. In contrast to EOF, for which a single mode defines a stationary oscillation, HSVD modes appear only in pairs; each pair represents propagating oscillations, such as the MJO (Zhang and Hendon 1997), if they satisfy a separation criterion. No stationary oscillation exists in individual HSVD modes. Unless one insists that stationary oscillations are part of the MJO, this exclusive identification of propagating signals by HSVD might be its most obvious advantage over EOF as a method of extracting the MJO. Based on the HSVD method, the first pair of leading modes separated from the rest was identified for both $\mathbf{P}_d$ and $\mathbf{P}_s$ individually and for their combination $\mathbf{P}'$ from all four TRMM datasets, confirming the existence of MJO signals in all these variables. Under the assumption that deep ($\mathbf{P}_d$) and shallow ($\mathbf{P}_s$) heating should be treated not as independent but as closely related variables in the context of the MJO, $\mathbf{P}'$, rather than $\mathbf{P}_d$ and $\mathbf{P}_s$ separately, was diagnosed in this study to extract MJO signals (section 3b).

d. MJO reconstruction

The two leading HSVD modes in pair for $\mathbf{P}'$ were taken to represent the MJO in the equatorial domain (longitude):

$$\mathbf{P}^{\mathrm{MJO}}(x,t) = \mathbf{X}(x)\mathbf{H}(t) = \begin{bmatrix} \mathbf{X}_{d1}(x) & \mathbf{X}_{d2}(x) \\ \mathbf{X}_{s1}(x) & \mathbf{X}_{s2}(x) \end{bmatrix} \begin{bmatrix} \mathbf{H}_1(t) \\ \mathbf{H}_2(t) \end{bmatrix}$$
$$= \begin{bmatrix} \mathbf{X}_{d1}(x)\mathbf{H}_1(t) + \mathbf{X}_{d2}(x)\mathbf{H}_2(t) \\ \mathbf{X}_{s1}(x)\mathbf{H}_1(t) + \mathbf{X}_{s2}(x)\mathbf{H}_2(t) \end{bmatrix}$$
$$= \begin{bmatrix} \mathbf{P}_d^{\mathrm{MJO}}(x,t) \\ \mathbf{P}_s^{\mathrm{MJO}}(x,t) \end{bmatrix}, \quad (2)$$

where $\mathbf{X}_{kn}(x)$ represents the HSVD eigenvectors and $\mathbf{H}_n(t)$ its PCs, with $k = d, s$ being the index of the deep and shallow REOF components and $n = 1, 2$ the index for the first two (first pair) HSVD modes. The vertical structure of the MJO can be recovered by combining $\mathbf{P}^{\mathrm{MJO}}$ with $\{\mathbf{R}\}$:

$$\mathbf{Q}^{\mathrm{MJO}}(x,z,t) = \{\mathbf{R}\}(z)\mathbf{P}^{\mathrm{MJO}}(x,t) = [\{\mathbf{R}_d\}(z)\ \{\mathbf{R}_s\}(z)] \begin{bmatrix} \mathbf{P}_d^{\mathrm{MJO}}(x,t) \\ \mathbf{P}_s^{\mathrm{MJO}}(x,t) \end{bmatrix}$$
$$= \{\mathbf{R}_d\}(z)\mathbf{P}_d^{\mathrm{MJO}}(x,t) + \{\mathbf{R}_s\}(z)\mathbf{P}_s^{\mathrm{MJO}}(x,t)$$
$$= \{\mathbf{R}_d\}(z)[\mathbf{X}_{d1}(x)\mathbf{H}_1(t) + \mathbf{X}_{d2}(x)\mathbf{H}_2(t)] + \{\mathbf{R}_s\}(z)[\mathbf{X}_{s1}(x)\mathbf{H}_1(t) + \mathbf{X}_{s2}(x)\mathbf{H}_2(t)]$$
$$= \mathbf{Q}_d^{\mathrm{MJO}}(x,z,t) + \mathbf{Q}_s^{\mathrm{MJO}}(x,z,t), \quad (3)$$

where $\mathbf{Q}_d^{\mathrm{MJO}}(x, z, t)$ and $\mathbf{Q}_s^{\mathrm{MJO}}(x, z, t)$ represent MJO signals in latent heating associated with the deep and shallow components, $\mathbf{Q}_d$ and $\mathbf{Q}_s$, respectively.

e. MJO composite

Composites (indicated by a caret) can be made for each of the MJO phases ($m = 1, 2, \ldots$) using reconstructed heating of the deep component,

$$\hat{\mathbf{Q}}_d^{\mathrm{MJO}}(x,z,m) = \sum_{t\in m} \mathbf{Q}_d^{\mathrm{MJO}}(x,z,t) = \{\mathbf{R}_d\}(z)\hat{\mathbf{P}}_d^{\mathrm{MJO}}(x,m), \quad (4a)$$

the shallow component,

$$\hat{\mathbf{Q}}_s^{\mathrm{MJO}}(x,z,m) = \sum_{t\in m} \mathbf{Q}_s^{\mathrm{MJO}}(x,z,t) = \{\mathbf{R}_s\}(z)\hat{\mathbf{P}}_s^{\mathrm{MJO}}(x,m), \quad (4b)$$

or their combination,

$$\hat{\mathbf{Q}}_{ds}^{\mathrm{MJO}}(x,z,m) = \hat{\mathbf{Q}}_d^{\mathrm{MJO}}(x,z,m) + \hat{\mathbf{Q}}_s^{\mathrm{MJO}}(x,z,m). \quad (4c)$$

Without the deep and shallow decomposition, composites can be made using total heating $\mathbf{Q}$,

$$\hat{\mathbf{Q}}_{\mathrm{total}}^{\mathrm{MJO}}(x,z,m) = \sum_{t\in m} \mathbf{Q}(x,z,t), \quad (4d)$$

or its intraseasonal anomalies,

$$\hat{\mathbf{Q}}_{\mathrm{intra}}^{\mathrm{MJO}}(x,z,m) = \sum_{t\in m} \mathbf{Q}'(x,z,t). \quad (4e)$$

MJO phases can be defined using any MJO index. In this study, we first used the HSVD time series $\mathbf{H}_1(t)$ and $\mathbf{H}_2(t)$ to define MJO phases. To reduce uncertainties due to small amplitudes of $\mathbf{H}_1(t)$ and $\mathbf{H}_2(t)$, defined as $A_{\mathbf{H}}(t) = [\mathbf{H}_1(t)^2 + \mathbf{H}_2(t)^2]^{1/2}$, composites were made only when $A_{\mathbf{H}}(t) > A_{\mathbf{H}0}$, where $A_{\mathbf{H}0}$ is a threshold. The Real-Time Multivariate MJO (RMM) index of Wheeler and Hendon (2004) was also used (section 3d).

3. Results

Before applying any diagnostic tool, we first demonstrate that MJO signals can be seen in the latent heating data of TRMM without any statistical manipulation. Figure 4 shows time–longitude diagrams of vertically averaged latent heating in the tropics (15°S–15°N) for an arbitrarily chosen period. Eastward propagation of concentrated heating at a speed of roughly 5 m s^{-1} (black straight lines) can be seen over the Indian and western Pacific Oceans and sometimes farther eastward with smaller amplitudes. This is no surprise. The spatial distribution and temporal variability of vertically averaged latent heating must match those of surface precipitation. MJO signals can be seen in precipitation without any statistical assistance (Zhang 2005). The most obvious differences among the four datasets are in their amplitudes. This results partially from different surface precipitation estimates (PR based for SLH, CSH, and PRH versus TMI based for TRN) used to determine the amplitudes of latent heating, and partially from details in the latent heating algorithms (e.g., underestimation of convective heating in the lower troposphere by PRH). Despite these discrepancies, the visible MJO signals in unfiltered latent heating data of TRMM assure that the results shown in the rest of this section are not statistical artifacts.

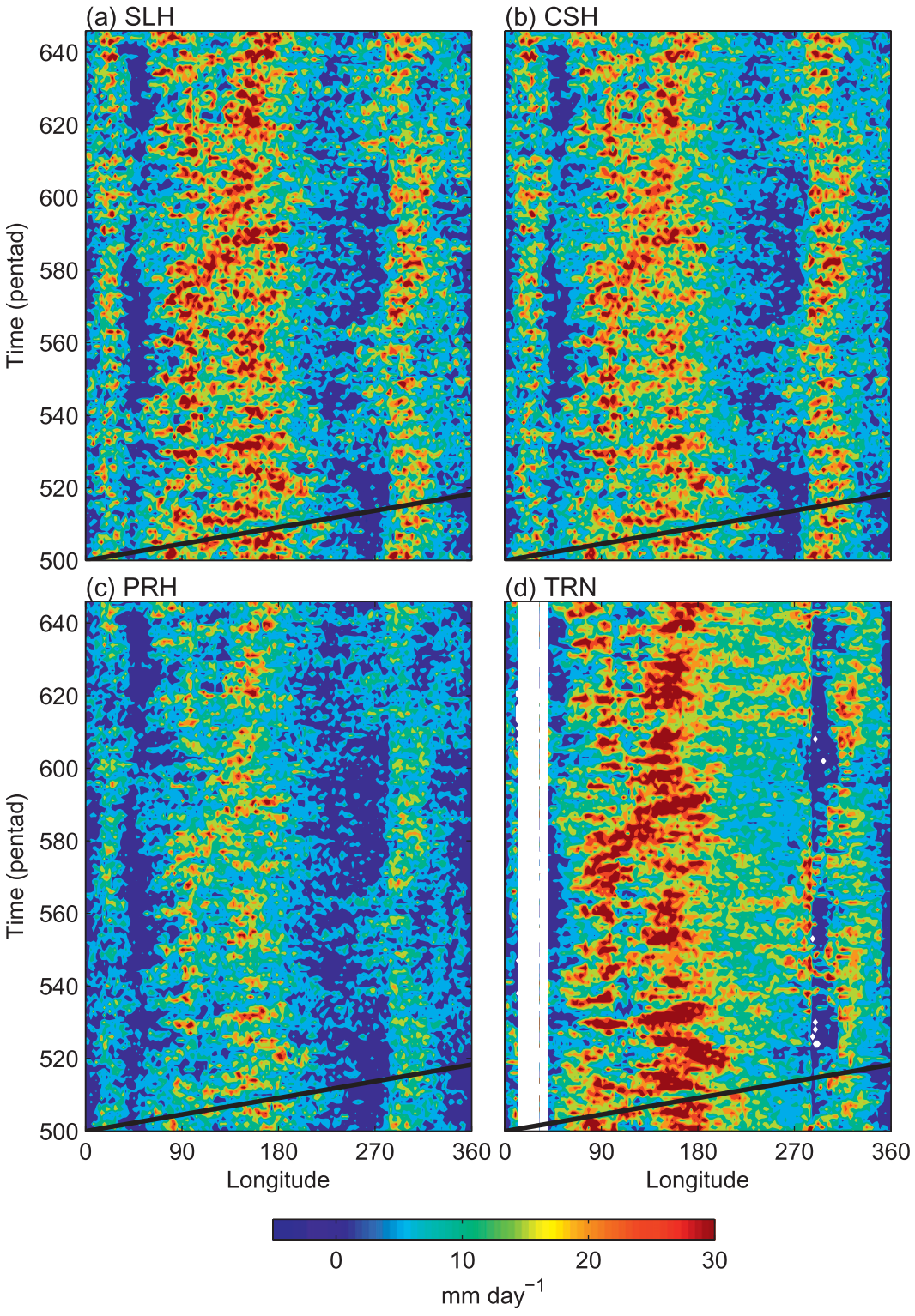

FIG. 4. Time–longitude diagrams of vertically averaged tropical (15°S–15°N) Q (K day^{-1}) for an arbitrary period. The black straight lines mark eastward propagation of 5 m s^{-1}.

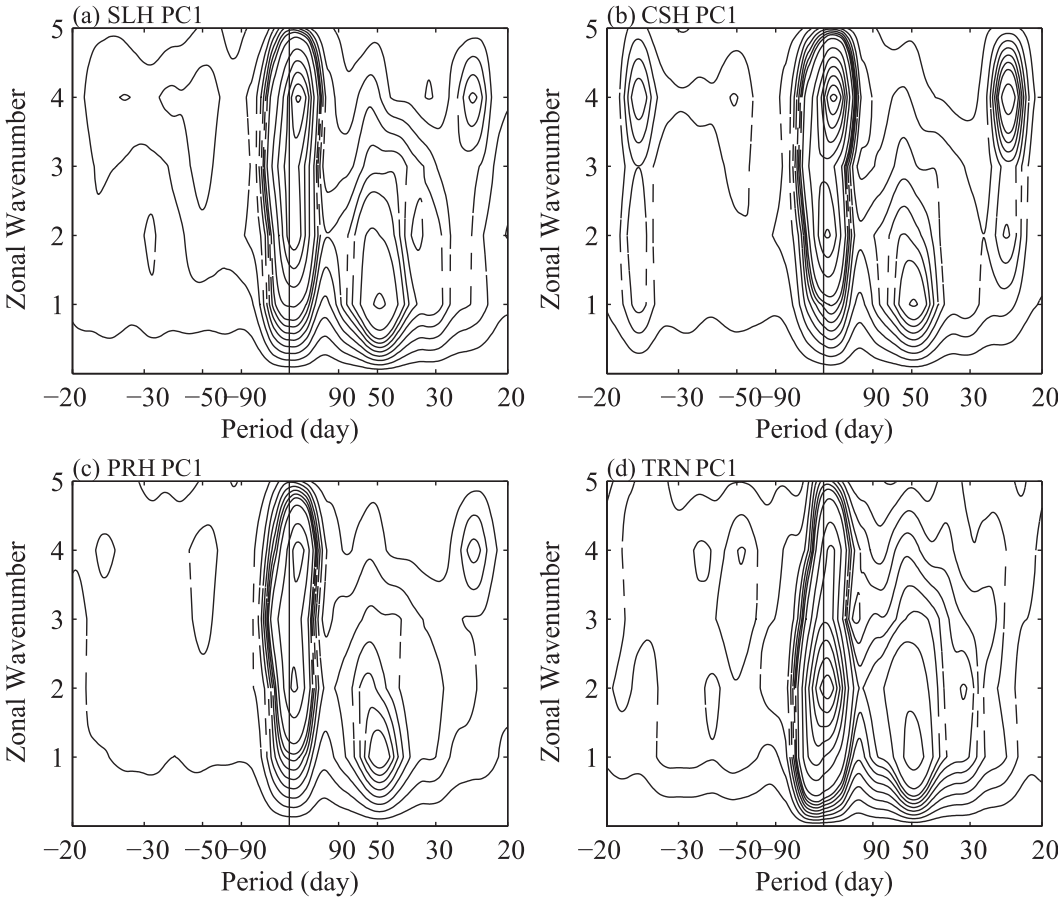

FIG. 5. Time–space spectra of $\mathbf{P}_d(x, t)$ (REOF PC1). Amplitudes are scaled for best visual effects.

a. Spectrum

The MJO is such a prominent intraseasonal phenomenon that without any filtering its signal can be easily identified from total time–space spectra of zonal wind and precipitation (or OLR) as eastward spectral peaks that are well distinguished from lower- and higher-frequency power and much stronger than their westward counterparts (Zhang 2005). This is the case for TRMM latent heating datasets as well. Figures 5 and 6 show time–space spectra of the PCs of the deep and shallow components of heating anomalies [i.e., $\mathbf{P}_d(x, t)$ and $\mathbf{P}_s(x, t)$] without any filtering except smoothing of the contours. For the deep component (Fig. 5), all four TRMM datasets exhibit robust MJO spectral peaks centered at an eastward (positive) period of 50 days and zonal wavenumber 1, as seen in precipitation. The MJO spectral signals for the shallow component (Fig. 6) are less prominent. There is stronger westward intraseasonal power in SLH and TRN. The eastward intraseasonal power in PRH is weak but still discernable. Nevertheless, similar to the deep component, the spectral peaks of the shallow component are all centered near 50 days and zonal wavenumber 1. These spectra unambiguously indicate the existence of MJO signals in the deep and shallow components of the TRMM latent heating datasets and therefore justify the application of intraseasonal filtering to further isolate the MJO signals as described in section 2c.

There are spectral peaks at higher frequencies (period $\approx$ 23 days) at zonal wavenumbers 2–4 for the shallow components, which are particularly strong in SLH and PRH. They also exist in the spectrum for the deep component of CSH. They have comparable amplitudes at the positive and negative frequencies, implying a possible stationary nature. These spectral peaks are likely to be unphysical, caused by the aliasing of the diurnal cycle onto the 23-day repeat cycle of TRMM's precessing orbit (Negri et al. 2002). Their existence, however, does not affect the diagnosis of the MJO. They are not included in the intraseasonally band-passed (30–90 days) anomalous time series used in the rest of the study. In fact, similar results were obtained from 20–90-day band-pass filtered time series.

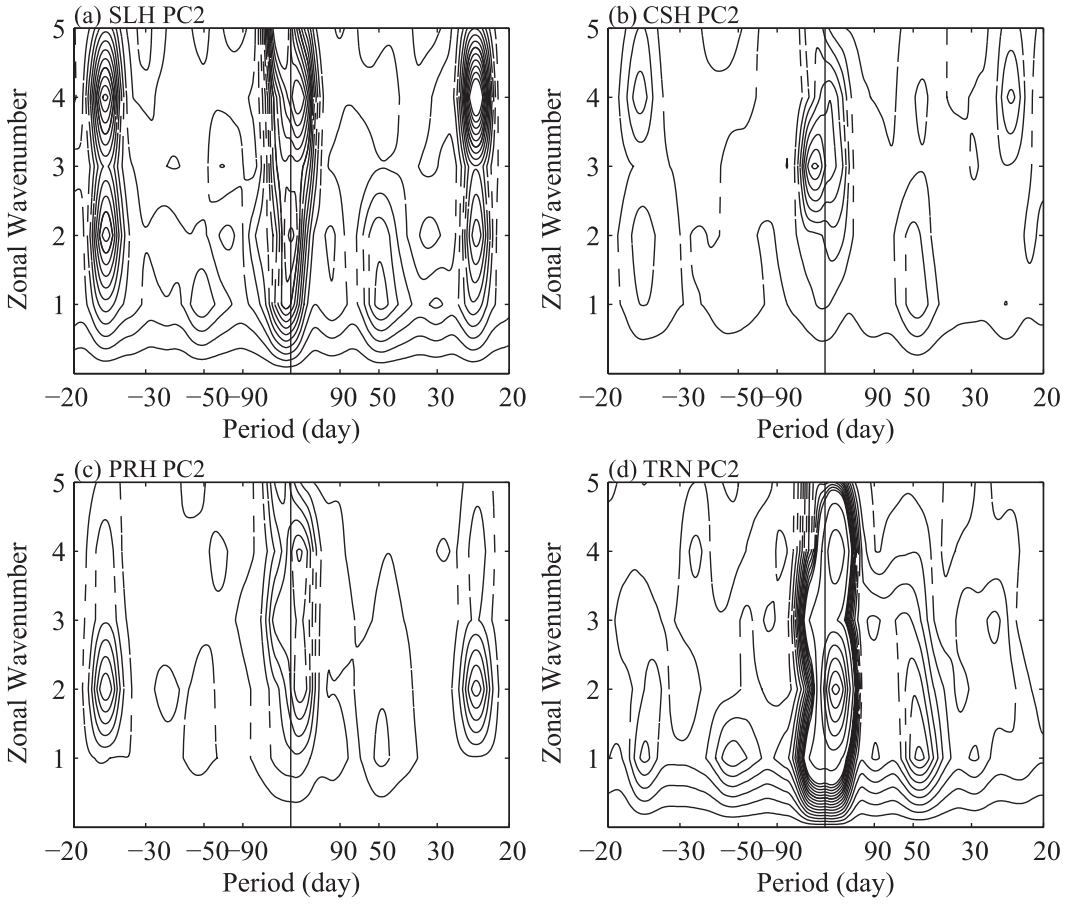

FIG. 6. As in Fig. 5, but for $\mathbf{P}_s(x, t)$ (REOF PC2).

b. HSVD modes

As described in section 2c, MJO signals were extracted from total intraseasonal heating using an HSVD analysis applied to the deep and shallow components combined. The first two HSVD modes are well separated from their neighboring modes according to the North et al. (1982) criterion. Their zonal scale (zonal wavenumber 1–2) matches well that of the known MJO scales, and their fractional variances are 74% (SLH), 73% (CSH), 76% (PRH), and 79% (TRN), respectively. These two modes together are taken to represent the MJO.

The third and fourth HSVD modes are also well separated from their neighboring higher modes. Their fractional variance is at most 12%. Their zonal scales (zonal wavenumber 4) are smaller than those of the first two modes and the MJO. Reconstructed heating based on the third and fourth modes propagate eastward in SLH and CSH, but westward in PRH and TRN. These two modes are not included in the MJO representation of this study. The physical interpretations for the third and fourth HSVD modes, if they are not artifacts, should be reported in a separate study.

For all four TRMM datasets, correlation between the PCs of the first two HSVD leading modes reaches maximum at a lag of about 2–3 pentads (not shown). This indicates a period of 40–60 days, consistent with the known MJO time scales and the spectra in Figs. 5 and 6. The eigenvectors of the two leading HSVD modes [see Eq. (2)] are shown in Fig. 7. In all four TRMM datasets, the eigenvectors for the deep component ($\mathbf{X}_{d1}$ and $\mathbf{X}_{d2}$) have significant amplitudes only over the Indian and western Pacific Oceans and the phases of the first and second HSVD modes are in quadrature with each other (Fig. 7, left panels). These are typical features in the eigenvectors of the leading modes for the MJO that can also be derived from other variables (e.g., Wheeler and Hendon 2004). The eigenvectors for the shallow component ($\mathbf{X}_{s1}$ and $\mathbf{X}_{s2}$) show less consistent structures and phase relationships across the four TRMM datasets (Fig. 7, right panels). Their quadrature phase relations are less obvious in some datasets (e.g., PRH) than others (e.g., CSH and TRN). This is another example

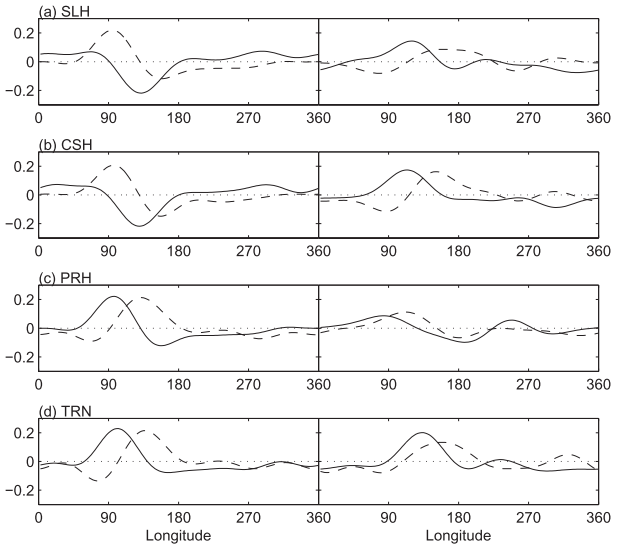

FIG. 7. Eigenvectors of the first ($n = 1$, solid) and second ($n = 2$, dashed) HSVD modes of the (left) $\mathbf{X}_{dn}$ and (right) $\mathbf{X}_{sn}$. Amplitudes are scaled for better comparison of the phases.

that the retrievals of heating due to shallow convection and warm rain by the four TRMM algorithms are not in complete agreement.

c. Variance

Zonal distributions of variance in the deep and shallow components of unfiltered latent heating are shown in Fig. 8, which was calculated using their REOF PCs ($\mathbf{P}_d$ and $\mathbf{P}_s$). The variability in the deep components is at least an order of magnitude greater than the shallow components. Whereas the vertical structures of the deep and shallow components of latent heating exhibit zonal ubiquity, as seen in Fig. 2, the amplitudes of their temporal fluctuations vary substantially in longitude. Three convective centers over the Indian Ocean–Maritime Continent–western Pacific, South America, and Africa are clearly seen in both deep and shallow components of latent heating. Three local minima are over the western Indian, eastern Pacific, and eastern Atlantic Oceans, all characterized with relatively low sea surface temperature (SST). This zonal distribution is expected from that of mean precipitation. The almost identical zonal distributions of the variance in the deep and shallow components, different amplitudes notwithstanding, suggest that they are both modulated by the same factors: zonal distributions of the land–sea contrast and SST.

Zonal distributions of variance in the deep and shallow components of MJO latent heating (e.g., $\mathbf{P}_d^{\mathrm{MJO}}$ and $\mathbf{P}_s^{\mathrm{MJO}}$) are shown in Fig. 9. As for the total heating, the variability of the deep components is an order of magnitude greater than the shallow components. For all four TRMM datasets, the strongest MJO heating, including

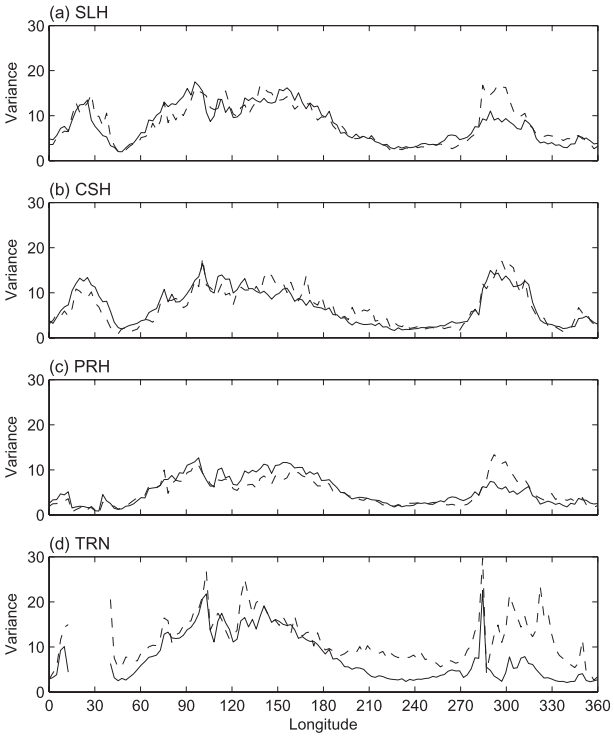

FIG. 8. Variance ($\mathrm{K}^2\ \mathrm{day}^{-2}$) of $\mathbf{P}_d$ (solid) and $\mathbf{P}_s$ (dashed). The amplitudes of the shallow components are amplified 10 times (20 for SLH).

both its deep and shallow components, is confined to the Indian and western/central Pacific Oceans. There is an obvious local minimum in the deep components over the Maritime Continent in all four datasets. The exact longitude of this minimum varies only slightly. The strength of MJO latent heating is comparable over the eastern Indian and western Pacific Oceans. The Maritime Continent minimum is a unique feature of the MJO, also seen in its precipitation (Waliser et al. 2009). No such minimum over the Maritime Continent in the variance of total latent heating can be clearly identified (Fig. 8). MJO heating in other equatorial regions is much weaker, despite strong total latent heating there, especially over tropical South America and Africa (Fig. 8). Robust MJO signals in wind and OLR along the intertropical convergence zone (ITCZ) have been detected over the eastern Pacific (Maloney and Esbensen 2003), but these signals are very local and relatively weak in the global MJO derived from the HSVD analysis. They are visible, however, as a secondary peak over the eastern Pacific in the variance of the deep component of total intraseasonal latent heating ($\mathbf{P}'_d$, not shown) and in the composite of total heating (section 3d).

Among the four TRMM datasets, the zonal distributions of the deep components of MJO latent heating

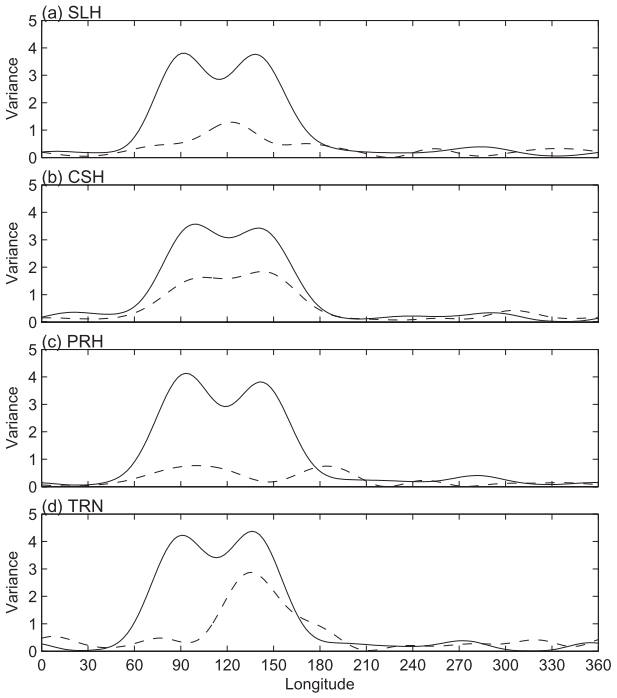

FIG. 9. As in Fig. 8, but for $\mathbf{P}_d^{\mathrm{MJO}}$ (solid) and $\mathbf{P}_s^{\mathrm{MJO}}$ (dashed). The amplitudes of the shallow components are amplified 20 times.

agree well. In contrast, distributions of the shallow components of MJO latent heating differ substantially, except for relatively large variability over eastern Indian and western Pacific Oceans. The peaks of their variance are located at different longitudes, with a single peak for SLH and TRN and double peaks for CSH and PRH. Figures 8 and 9 together imply, again, that uncertainties in the shallow components of the four TRMM datasets are larger than those in the deep components.

d. Composite

Reconstructed heating profiles of both deep and shallow components exhibit a systematic eastward propagation, as expected from their spectra (Figs. 5 and 6), from the Indian to central Pacific Oceans. Their phase relationships can be examined through composites of the REOF PCs, namely $\hat{\mathbf{P}}_d^{\mathrm{MJO}}(x, m)$ and $\hat{\mathbf{P}}_s^{\mathrm{MJO}}(x, m)$ for MJO phases ($m = 1, \ldots, 8$), based on Eqs. (4a) and (4b). These composites are shown in Fig. 10. MJO phases were defined using the HSVD PCs ($\mathbf{H}_1$ and $\mathbf{H}_2$) in a similar way as using the RMM index in Wheeler and Hendon (2004). The amplitude threshold for the composite $A_{\mathbf{H}0}$ (section 2d) was set to 1.5 standard deviations of $A_{\mathbf{H}}$. For each dataset, $\mathbf{H}_1$ and $\mathbf{H}_2$ are unique. No effort was made to define the phase based on the longitudes of the maxima or minima of the composites.

The continuous eastward propagation in both deep and shallow components of all TRMM datasets starts over the Indian Ocean with amplitudes maintained through the western Pacific. As seen before, outside the Indian and western Pacific Ocean region, the deep components are very weak, but the shallow components exhibit visible variability over the eastern Pacific and Atlantic Oceans.

The relative phases of the shallow and deep components vary substantially among the four latent heating datasets. In three of them (SLH, CSH, and PRH), the shallow and deep components are almost completely out of phase over the Indian and western Pacific Oceans. One may get an impression that the shallow components lead (to the east of) the deep components. But this phase relationship is not nearly as clear as that observed for the MJO events during TOGA COARE and reconstructed using a multiyear global reanalysis time series (Lin et al. 2004; Kiladis et al. 2005), in which shallow heating immediately precedes (or is located east of) deep heating. This can be clearly seen only in TRN (Fig. 10d).

The phase relationship between the deep and shallow components can be further examined through composites at a given longitude following a different approach. First, ''major'' MJO events, defined as those with $A_{\mathbf{H}}$ greater than the standard deviation for at least 30 consecutive days, were selected. Those events were then made into composites over 50 days centered at the day of the heating peak at a given longitude reference point. Figures 11 and 12 show such composites at 90° and 150°E, respectively. They are very similar. The shallow components (contours) lead the deep ones (colors, left panels) by 15–20 days in all datasets but TRN, in which the lead is about 5 days. The maximum shallow cooling 5 days behind the deep heating maximum in SLH, CSH, and PRH may imply trailing stratiform precipitation. In the deep and shallow combined MJO heating field [$\hat{\mathbf{Q}}_{ds}^{\mathrm{MJO}}$ in Eq. (4c), right panels of Figs. 11 and 12], there is a sign of low-level heating preceding the main heating centers of the MJO but no visible indication of trailing stratiform-like upper-level heating following the main deep heating maxima. The level of the low-level heating varies among the datasets. It is the highest in PRH and lowest in CSH, as seen earlier. The subtle phase change related to low-level heating is more visible following the zero contours than following the amplitude (colors), mainly because the shallow component is much weaker than the deep one.

The composites in Figs. 10–12 are all based on the TRMM latent heating data alone. The purpose of this has been stated in section 1, which is to determine the MJO signals in latent heating independent of other variables. One might be concerned about information degeneration in such practice: the definition of the MJO and

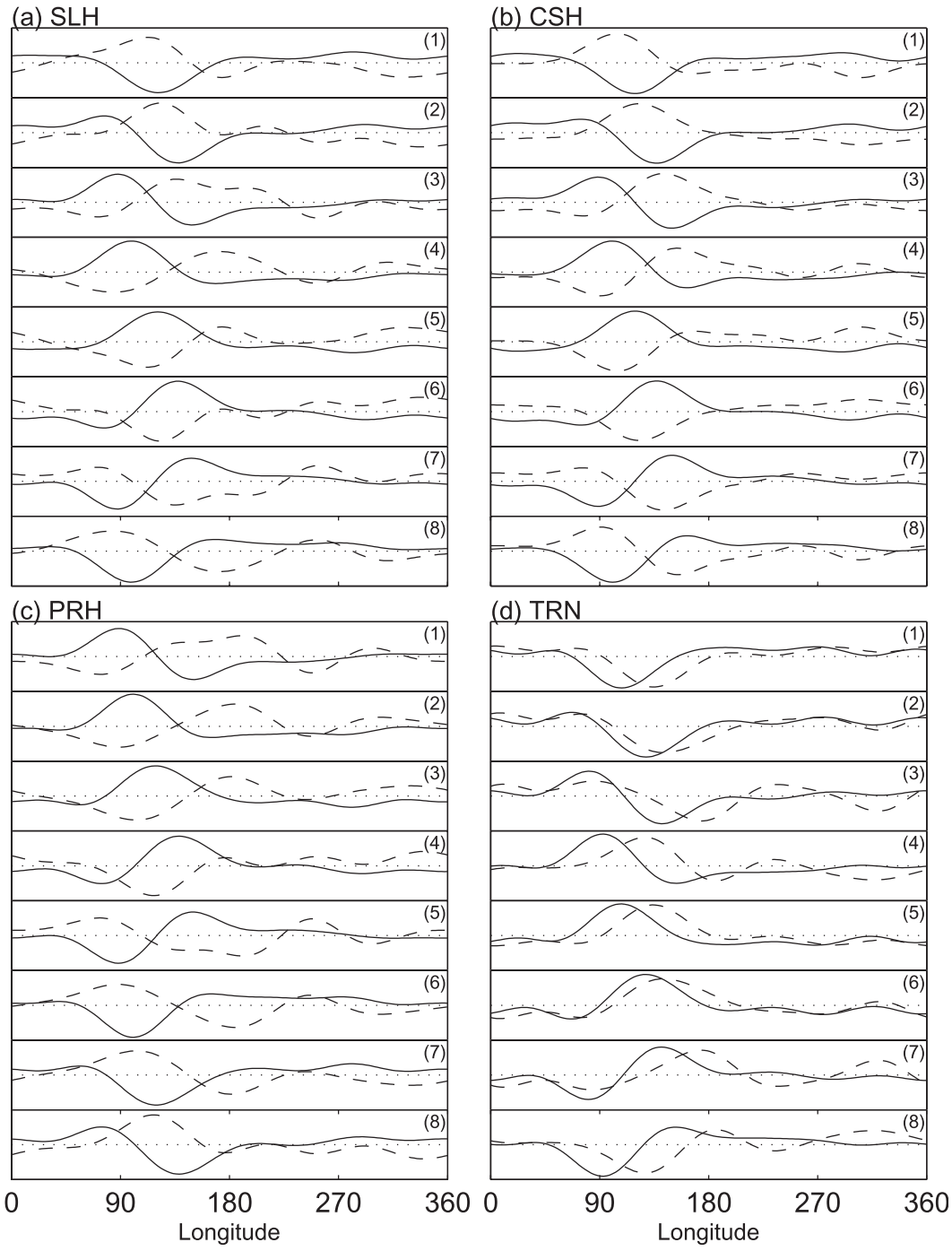

FIG. 10. Composite $\mathbf{P}_d^{\mathrm{MJO}}$ (solid) and $\mathbf{P}_s^{\mathrm{MJO}}$ (dashed) as functions of longitude and MJO phases (indicated in the upper right corners) defined by $\mathbf{H}_1$ and $\mathbf{H}_2$. Each curve was scaled by its standard deviation for a better visual effect of phase relationships.

the quantity made into the MJO composite are the same. Next, we relaxed our constraint in two ways: we used an independent MJO index, the RMM of Wheeler and Hendon (2004), to define the MJO phases and we used intraseasonal anomalous time series of the deep and shallow components combined ($\mathbf{Q}'_d + \mathbf{Q}'_s$) instead of the leading modes from the HSVD analysis. The only remaining constraint in the composites is the REOF decomposition of the deep and shallow components. The results are given in Fig. 13. The eastward propagation

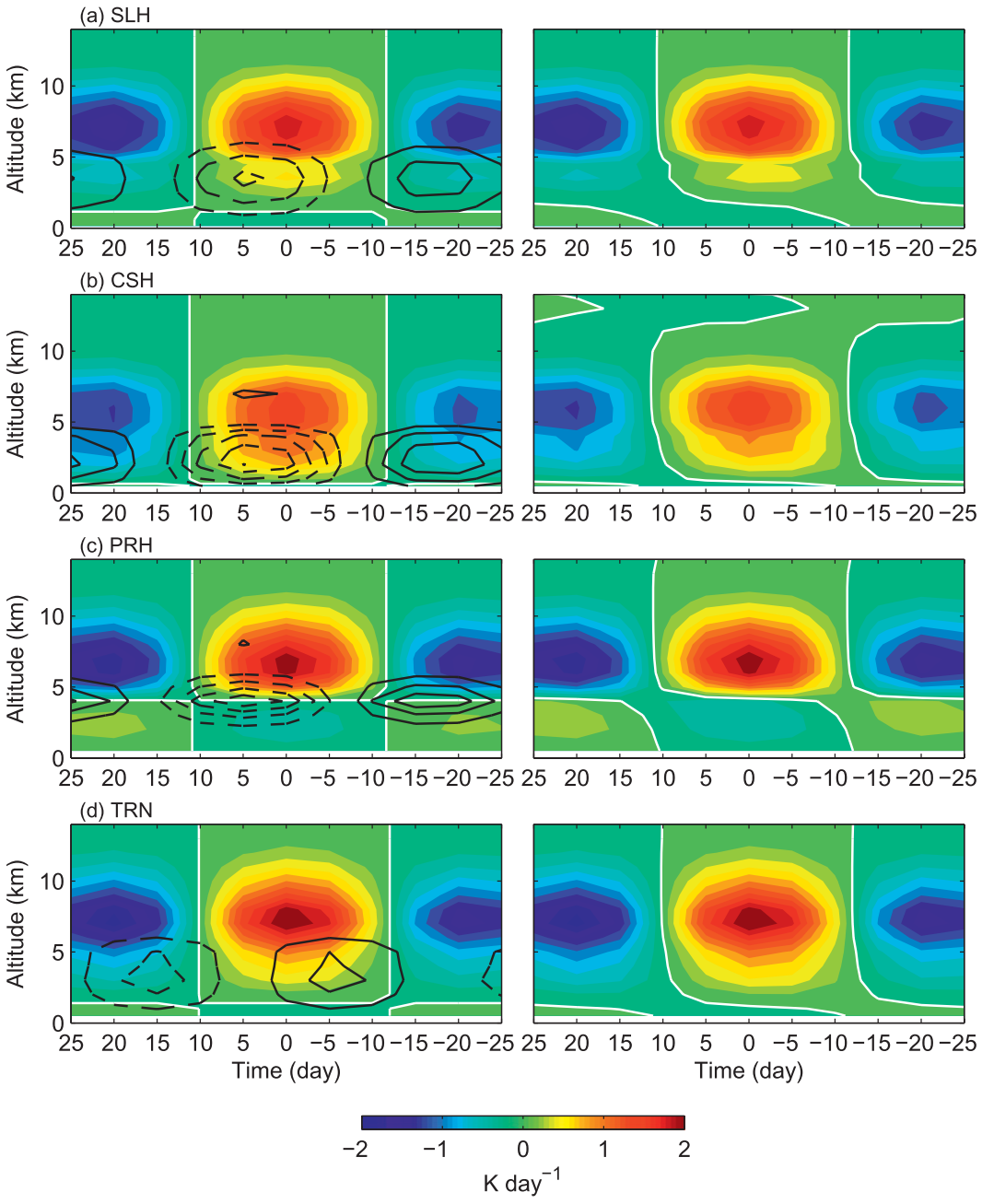

FIG. 11. Composite latent heating profiles (K day^{-1}) as functions of time at 90°E for (left) the deep (colors) and shallow (contour interval = 0.05 K day^{-1}) components and (right) deep and shallow components combined. Zeros are marked by white contours.

and the deep heating structures of the four datasets agree well with each other in general. Interestingly, the local minimum over the Maritime Continent seen in the variance of the deep components (Fig. 9) is manifested here as a temporary weakening of the deep heating peak in phase 4. There are secondary deep heating peaks over the eastern Pacific, likely related to the MJO activity there (Maloney and Esbensen 2003), which propagate into the Atlantic. This eastern Pacific MJO coexists with the MJO over the western Pacific and the two propagate eastward simultaneously in a semi-synchronized fashion in phases 6, 7, 8, and 1. The eastern Pacific MJO is thus distinguished from the western Pacific MJO but may be triggered by the latter (Small et al. 2010).

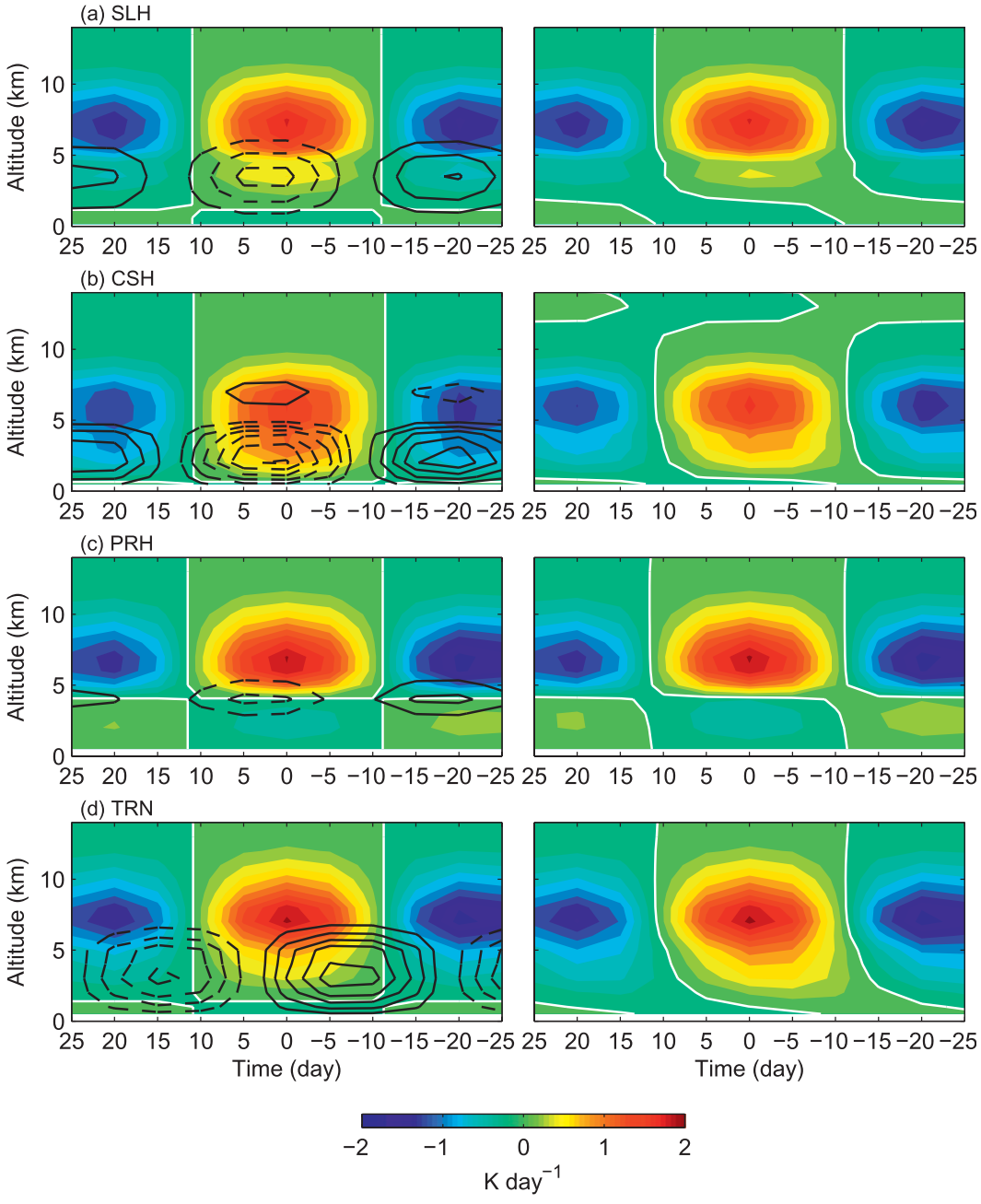

FIG. 12. As in Fig. 11, but at 150°E.

Shallow heating preceding deep heating seen from the previous composites is also shown in Fig. 13. Again, it is easier to see by following the zero contours than the colors (amplitude) because of the weak shallow components. This structural evolution is more visible in SLH and TRN than the other two and exists only over the Indian and western Pacific Oceans. There is no such structural evolution over the eastern Pacific Ocean even though eastward propagating signals representing the MJO are evident there.

4. Summary and discussion

Motivated by the potential importance of structural evolution of latent heating to MJO dynamics (section 1), we examined and compared MJO signals in four latent

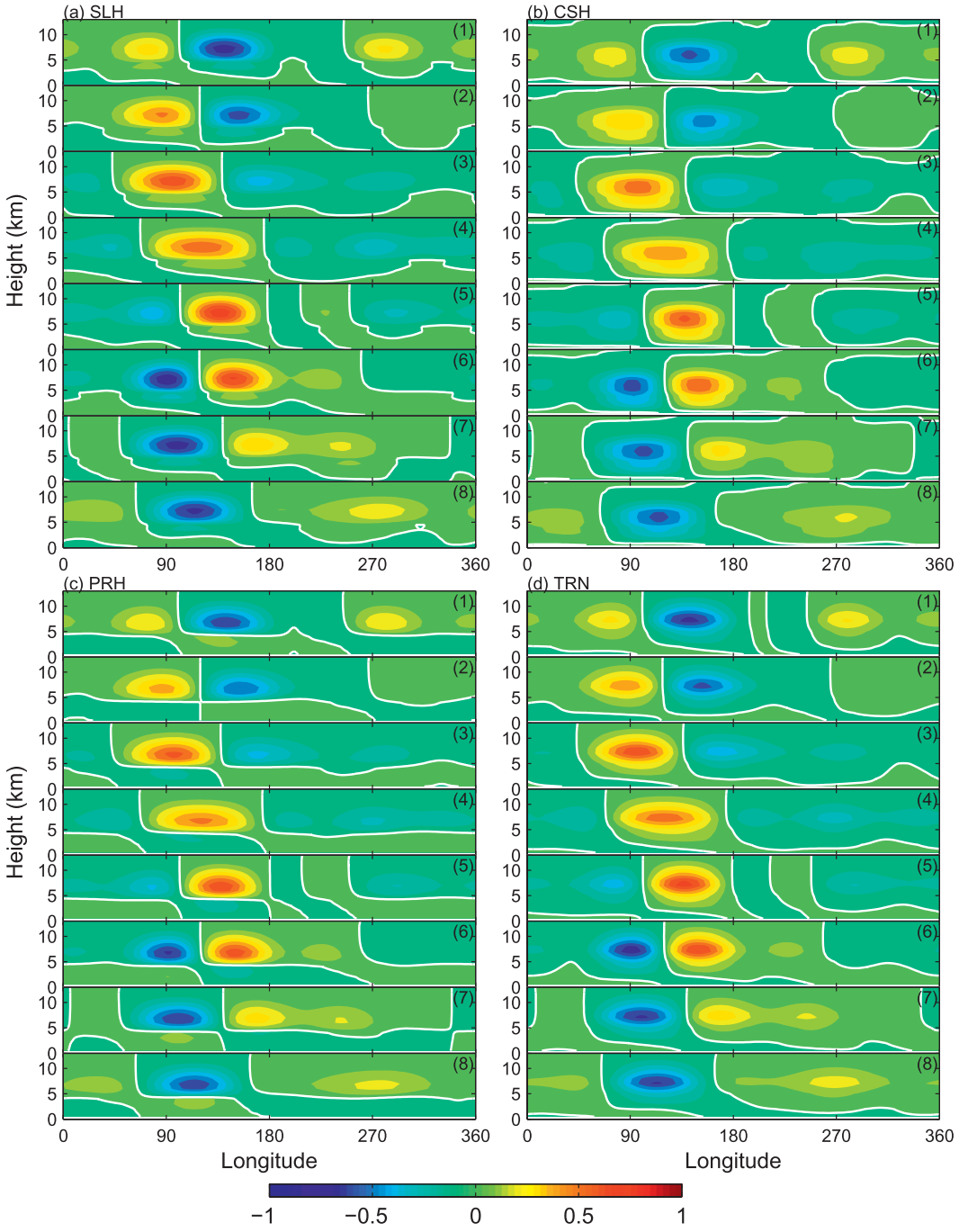

FIG. 13. Composites of intraseasonal anomalous latent heating (K day^{-1}) with the deep and shallow components combined as functions of longitude and MJO phases (indicated in the upper right corners) defined by the RMM index (Wheeler and Hendon 2004). Zeros are marked by white contours.

heating datasets derived from TRMM observations. Similarities in these datasets may lend us confidence in their credibility. Their discrepancies, due to differences in their algorithms, point to the uncertainties and need for improvement in the datasets and the caution that must be exercised in their applications.

The gross vertical structure of latent heating in the tropics (averaged between 15°S and 15°N) and its variability can be well represented by the eigenvectors of the two leading REOF components, one deep with its peak above the melting level and one shallow with its peak below (Fig. 1). The eigenvectors of the two leading

REOF components are nearly ubiquitous in longitude (Fig. 2). Almost all zonal and temporal variability in tropical latent heating resides in the principal components (PCs) (Fig. 3). This allows a separation of variables that decomposes the latent heating field in the tropics into two independent parts: its vertical structures represented by the deep and shallow components, and its longitudinal and temporal variability represented by the PCs. Latent heating associated with the MJO can be diagnosed by first extracting MJO signals from its zonal and temporal variability and then recovering its vertical structures using the REOF eigenvectors (i.e., the deep and shallow components).

Following this approach, we have focused on the structural variability in latent heating of the MJO in longitude and time. The main results are as follows:

1) There are clear spectral signals of the MJO in both deep and shallow components of latent heating. The intraseasonal (50 days), planetary-scale (zonal wavenumber 1), and eastward moving spectral peaks are well distinct from spectral power at lower and higher frequencies. The spectral signal of the MJO is much more robust (much stronger than the corresponding westward power) in the deep component than the shallow one (Figs. 5 and 6). MJO signals in deep and shallow components of latent heating were successfully extracted from their intraseasonal anomalies by an HSVD analysis.
2) The strongest MJO signals in both deep and shallow components of latent heating are confined to the Indian and western Pacific Oceans. Deep components exhibit an obvious local minimum over the Maritime Continent. Detailed zonal distributions of the MJO shallow components of the four TRMM datasets, however, disagree substantially (Fig. 9).
3) There are signs of the shallow component immediately leading (to the east of) the deep component. However, this is obvious only in certain datasets at certain longitudes (Figs. 10 and 13).
4) MJO signals propagating from the eastern Pacific to the Atlantic coexist in synchronization with those over the western Pacific (Fig. 13).

These results lead to several implications. The strong evidence of MJO signals in latent heating provides justification for using it in combination with other variables to seek their coherence in the context of the MJO (e.g., Morita et al. 2006; Lau and Wu 2010). The synchronized coexistence of the western and eastern Pacific MJO during a half of the life cycle of the global MJO may explain the extension of the MJO spectral peak from zonal wavenumber 1 to 2 (Fig. 5) and also suggests that the former may act to trigger the latter. The consistent behaviors of the MJO signal in the deep component in all four latent heating datasets, compatible with the expectation based on known MJO signatures in precipitation, suggest the reliability of these datasets in detecting latent heating due to deep convective cloud systems. In contrast, the disagreements among the four datasets in the shallow components in general (their mean vertical profiles in Figs. 1 and 2), in their zonal distributions (Fig. 8), and in their MJO signals (the eigenvectors in Fig. 7 and the variance distributions in Fig. 9) indicate that the challenge of retrieving latent heating by shallow, warm-rain cloud systems has yet to be met.

The previously reported vertical tilt in MJO latent heating (Lin et al. 2004; Kiladis et al. 2005) is not confirmed without ambiguity in this study. Such tilt consists of two features: shallow heating preceding (to the east of) main deep heating in the MJO convection center, and trailing stratiform-like heating in the upper troposphere behind (to the west of) the MJO convection center. Shallow heating leading deep heating can indeed be found but only in some TRMM datasets and at certain longitudes. No trailing stratiform-like heating behind (west of) the main heating center of the MJO is detected in this study. There are several possible explanations for this. First, the westward tilt was previously reported in total diabatic heating. Radiative heating could contribute significantly to the total diabatic heating when the precipitation rate is low and latent heating is relatively weak during the transition period from convectively inactive to active phases of the MJO. If so, latent heating alone may not yield the tilt. Two TRMM datasets (CSH and TRN) provide both latent heating and total diabatic heating. We applied the same diagnosis to their total diabatic heating and the results are not visibly distinguishable from those of latent heating. MJO signals from the radiative heating component Q_R cannot be diagnosed using the same approach. It does not have any zonally ubiquitous deep or shallow components.

Second, the westward tilt in latent heating may occur only to a subset of MJO events, which happened to include those observed by the TOGA COARE data used in the previous reports (Lin et al. 2004; Kiladis et al. 2005). This possibility is implied by recent case studies using two TRMM latent heating datasets (TRN and an earlier version of CSH), two data assimilation products over a season with multiple MJO events (Jiang et al. 2009), and in situ sounding observations from the Indian Ocean for a particular MJO event (Katsumata et al. 2009). These studies did not find any obvious shallow leading deep heating in latent or total diabatic heating profiles during individual MJO events. If this is the case,

we should not expect a strong signal of the tilt in our composites.

Third, as discussed before, deficiencies in retrieving shallow heating from TRMM observations may make them unsuitable for detecting the structural evolution through the life cycle of the MJO. Other TRMM observations have, however, shown clearly that shallow convection tends to lead deep convection in the MJO life cycle (Kikuchi and Takayabu 2004; Masunaga et al. 2005; Lau and Wu 2010). This strongly suggests a systematic structural change in the latent heating field that is consistent with the westward tilt. More careful comparisons between TRMM retrievals of latent heating and other measures of convective cloud properties may yield useful information on this.

Finally, the decomposition into the deep and shallow components may not be adequate to fully resolve the structural evolution in latent heating. Higher modes may be needed to represent stratiform-like heating in the upper troposphere. When the same REOF decomposition of deep and shallow heating was applied to total diabatic heating profiles based on sounding observations, a shallow–deep stratiform heating structural sequence was clearly resolved, but not specifically for the MJO (Zhang and Hagos 2009).

To further address some of these issues, we are currently examining the latent heating structure and evolution associated with the MJO using a different approach: comparing latent and total diabatic heating fields (no deep versus shallow decomposition) from TRMM and global reanalysis products, scrutinizing latent heating structures in individual MJO events in detail during and outside the TOGA COARE period, and combining latent heating with other variables deemed important to MJO dynamics. Results will be reported separately.

This article demonstrates the utility and uncertainty of TRMM latent heating retrievals in the study of the MJO and calls for further scrutiny of the issue regarding the structural evolution of latent heating through the life cycle of the MJO. In our view, whether shallow heating immediately preceding MJO convection centers and stratiform-like heating immediately following them are essential features of the MJO and whether they play indispensible roles in MJO dynamics remain as open questions.

Acknowledgments. The authors thank David Raymond and two anonymous reviewers for their constructive comments, which helped improve the presentation of this study. This study was supported by NASA Grant NNX07AD41G.

REFERENCES

Benedict, J. J., and D. A. Randall, 2007: Observed characteristics of the MJO relative to maximum rainfall. *J. Atmos. Sci.,* **64,** 2332–2354.

Chang, C.-P., 1977: Viscous internal gravity waves and low-frequency oscillations in the tropics. *J. Atmos. Sci.,* **34,** 901–910.

——, and H. Lim, 1988: Kelvin wave-CISK: A possible mechanism for the 30–50-day oscillations. *J. Atmos. Sci.,* **45,** 1709–1720.

Fu, X., and B. Wang, 2009: Critical roles of the stratiform rainfall in sustaining the Madden–Julian oscillation: GCM experiments. *J. Climate,* **22,** 3939–3959.

Grecu, M., and W. S. Olson, 2006: Bayesian estimation of precipitation from satellite passive microwave observations using combined radar–radiometer retrievals. *J. Appl. Meteor. Climatol.,* **45,** 416–433.

——, ——, C.-L. Shie, T. S. L'Ecuyer, and W.-K. Tao, 2009: Combining satellite microwave radiometer and radar observations to estimate atmospheric latent heating profiles. *J. Climate,* **22,** 6356–6376.

Hagos, S., and Coauthors, 2010: Estimates of tropical diabatic heating profiles: Commonalities and uncertainties. *J. Climate,* **23,** 542–558.

Houze, R. A., Jr., 1997: Stratiform precipitation in regions of convection: A meteorological paradox? *Bull. Amer. Meteor. Soc.,* **78,** 2179–2196.

Jiang, X., and Coauthors, 2009: Vertical heating structures associated with the MJO as characterized by TRMM estimates, ECMWF reanalyses and forecasts: A case study during 1998/99 winter. *J. Climate,* **22,** 6001–6020.

Johnson, R. H., and X. Lin, 1997: Episodic trade-wind regimes over the western Pacific warm pool. *J. Atmos. Sci.,* **54,** 2020–2034.

——, T. M. Rickenbach, S. A. Rutledge, P. E. Ciesielski, and W. H. Schubert, 1999: Trimodal characteristics of tropical convection. *J. Climate,* **12,** 2397–2418.

Kaiser, H. F., 1958: The varimax criterion for analytic rotation in factor analysis. *Psychometrika,* **23,** 187–200.

Katsumata, M., R. H. Johnson, and P. E. Ciesielski, 2009: Observed synoptic-scale variability during the developing phase of an ISO over the Indian Ocean during MISMO. *J. Atmos. Sci.,* **66,** 3434–3448.

Khouider, B., and A. J. Majda, 2006: A simple multicloud parameterization for convectively coupled tropical waves. Part I: Linear analysis. *J. Atmos. Sci.,* **63,** 1308–1323.

——, and ——, 2008: Multicloud models for organized tropical convection: enhanced congestus heating. *J. Atmos. Sci.,* **65,** 895–914.

Kikuchi, K., and Y. N. Takayabu, 2004: The development of organized convection associated with the MJO during TOGA COARE IOP: Trimodal characteristics. *Geophys. Res. Lett.,* **31,** L10101, doi:10.1029/2004GL019601.

Kiladis, G. N., K. H. Straub, and P. T. Haertel, 2005: Zonal and vertical structure of the Madden–Julian oscillation. *J. Atmos. Sci.,* **62,** 2790–2809.

Kodama, Y.-M., M. Katsumata, S. Mori, S. Satoh, Y. Hirose, and H. Ueda, 2009: Climatology of warm rain and associated latent heating derived from TRMM PR observations. *J. Climate,* **22,** 4908–4929.

Kummerow, and Coauthors, 2000: The status of the Tropical Rainfall Measuring Mission (TRMM) after two years in orbit. *J. Appl. Meteor.,* **39,** 1965–1982.

Lau, W. K.-M., and D. E. Waliser, 2005: *Intraseasonal Variability of the Atmosphere–Ocean Climate System*. Springer, 474 pp.

——, and H.-T. Wu, 2010: Characteristics of precipitation, cloud, and latent heating associated with the Madden–Julian oscillation. *J. Climate,* **23,** 504–518.

L'Ecuyer, T. S., and G. L. Stephens, 2003: The tropical oceanic energy budget from the TRMM perspective. Part I: Algorithm and uncertainties. *J. Climate,* **16,** 1967–1985.

——, and ——, 2007: The tropical atmospheric energy budget from the TRMM perspective. Part II: Evaluating GCM representations of the sensitivity of regional energy and water cycles to the 1998–99 ENSO cycle. *J. Climate,* **20,** 4548–4571.

Li, C., X. Jia, J. Ling, W. Zhou, and C. Zhang, 2009: Sensitivity of MJO simulations to convective heating profiles. *Climate Dyn.,* **32,** 167–187.

Lin, J., B. E. Mapes, M. Zhang, and M. Newman, 2004: Stratiform precipitation, vertical heating profiles, and the Madden–Julian oscillation. *J. Atmos. Sci.,* **61,** 296–309.

López Carrillo, C., and D. J. Raymond, 2005: Moisture tendency equations in a tropical atmosphere. *J. Atmos. Sci.,* **62,** 1601–1613.

Madden, R. A., and P. R. Julian, 1971: Detection of a 40–50-day oscillation in the zonal wind in the tropical Pacific. *J. Atmos. Sci.,* **28,** 702–708.

——, and ——, 1972: Description of global-scale circulation cells in the tropics with a 40–50-day period. *J. Atmos. Sci.,* **29,** 1109–1123.

——, and ——, 1994: Observations of the 40–50-day tropical oscillation: A review. *Mon. Wea. Rev.,* **112,** 814–837.

Maloney, E. D., 2009: The moist static energy budget of a composite tropical intraseasonal oscillation in a climate model. *J. Climate,* **22,** 711–729.

——, and S. K. Esbensen, 2003: The amplification of east Pacific Madden–Julian oscillation convection and wind anomalies during June–November. *J. Climate,* **16,** 3482–3497.

——, D. B. Chelton, and S. K. Esbensen, 2008: Subseasonal SST variability in the tropical eastern North Pacific during boreal summer. *J. Climate,* **21,** 4149–4167.

Mapes, B. E., 2001: Water's two height scales: The moist adiabat and the radiative troposphere. *Quart. J. Roy. Meteor. Soc.,* **127,** 2253–2266.

Masunaga, H., T. S. L'Ecuyer, and C. D. Kummerow, 2005: Variability in the characteristics of precipitation systems in the tropical Pacific. Part I: Spatial structure. *J. Climate,* **18,** 823–840.

——, M. Satoh, and H. Miura, 2008: A joint satellite and global cloud-resolving model analysis of a Madden–Julian oscillation event: Model diagnosis. *J. Geophys. Res.,* **113,** D17210, doi:10.1029/2008JD009986.

Matsuno, T., 1966: Quasi-geostrophic motions in the equatorial area. *J. Meteor. Soc. Japan,* **44,** 25–43.

Morita, J., Y. N. Takayabu, S. Shige, and Y. Kodama, 2006: Analysis of rainfall characteristics of the Madden–Julian oscillation using TRMM satellite data. *Dyn. Atmos. Oceans,* **42,** 107–126.

Neelin, J. D., and I. M. Held, 1987: Modeling tropical convergence based on the moist static energy budget. *Mon. Wea. Rev.,* **115,** 3–12.

Negri, A. J., T. L. Bell, and L. Xu, 2002: Sampling of the diurnal cycle of precipitation using TRMM. *J. Atmos. Oceanic Technol.,* **19,** 1333–1344.

Nitta, T., and S. Esbensen, 1974: Heat and moisture budget analyses using BOMEX data. *Mon. Wea. Rev.,* **102,** 17–28.

North, G. R., T. L. Bell, R. F. Cahalan, and F. J. Moeng, 1982: Sampling errors in the estimation of empirical orthogonal functions. *Mon. Wea. Rev.,* **110,** 699–706.

Raymond, D. J., and Z. Fuchs, 2009: Moisture modes and the Madden–Julian oscillation. *J. Climate,* **22,** 3031–3046.

——, S. L. Sessions, A. H. Sobel, and Z. Fuchs, 2009: The mechanics of gross moist stability. *J. Adv. Model. Earth Syst.,* **1** (9), 1–20.

Schumacher, C., and R. A. Houze Jr., 2003: Stratiform rain in the tropics as seen by the TRMM precipitation radar. *J. Climate,* **16,** 1739–1756.

Shie, C.-L., W.-K. Tao, J. Simpson, and C.-H. Sui, 2003: Quasi-equilibrium states in the tropics simulated by a cloud-resolving model. Part I: Specific features and budget analysis. *J. Climate,* **16,** 817–833.

Shige, S., Y. N. Takayabu, W.-K. Tao, and D. E. Johnson, 2004: Spectral retrieval of latent heating profiles from TRMM PR data. Part I: Development of a model-based algorithm. *J. Appl. Meteor.,* **43,** 1095–1113.

——, ——, ——, and C.-L. Shie, 2007: Spectral retrieval of latent heating profiles from TRMM PR data. Part II: Algorithm improvement and heating estimates over tropical ocean regions. *J. Appl. Meteor. Climatol.,* **46,** 1098–1124.

——, ——, and ——, 2008: Spectral retrieval of latent heating profiles from TRMM PR data. Part III: Estimating apparent moisture sink profiles over tropical oceans. *J. Appl. Meteor. Climatol.,* **47,** 620–640.

——, ——, S. Kida, W.-K. Tao, X. Zeng, C. Yokoyama, and T. L'Ecuyer, 2009: Spectral retrieval of latent heating profiles from TRMM PR data. Part IV: Comparisons of lookup tables from two- and three-dimensional cloud-resolving model simulations. *J. Climate,* **22,** 5577–5594.

Small, R. J., S.-P. Xie, E. D. Maloney, S. P. de Szoeke, and T. Miyama, 2010: Intraseasonal variability in the far east Pacific: Investigation of the role of air–sea coupling in a regional coupled model. *Climate Dyn.,* doi:10.1007/s00382-010-0786-2, in press.

Sobel, A. H., Simple models of ensemble-averaged tropical precipitation and surface wind, given the sea surface temperature. *The Global Circulation of the Atmosphere,* T. Schneider and A. H. Sobel, Eds., Princeton University Press, 219–251.

Sui, C.-H., and K.-M. Lau, 1989: Origin of low-frequency (intraseasonal) oscillations in the tropical atmosphere. Part II: Structure and propagation of mobile wave-CISK modes and their modification by lower boundary forcings. *J. Atmos. Sci.,* **46,** 37–56.

Tao, W.-K., S. Lang, J. Simpson, and R. Adler, 1993: Retrieval algorithms for estimating the vertical profiles of latent heat release: Their applications for TRMM. *J. Meteor. Soc. Japan,* **71,** 685–700.

——, ——, ——, W. S. Olson, D. Johnson, B. Ferrier, C. Kummerow, and R. Adler, 2000: Vertical profiles of latent heat release and their retrieval for TOGA COARE convective systems using a cloud resolving model, SSM/I, and ship-borne radar data. *J. Meteor. Soc. Japan,* **78,** 333–355.

——, and Coauthors, 2006: Retrieval of latent heating from TRMM measurements. *Bull. Amer. Meteor. Soc.,* **87,** 1555–1572.

——, S. Lang, X. Zeng, S. Shige, and Y. Takayabu, 2010: Relating convective and stratiform rain to latent heating. *J. Climate,* **23,** 1874–1893.

Waliser, D. E., 2006: *Intraseasonal Variability: The Asian Monsoon.* Springer, 844 pp.

——, and Coauthors, 2009: MJO simulation diagnostics. *J. Climate,* **22,** 3006–3030.

Wang, B., 2005: Theory. *Intraseasonal Variability of the Atmosphere–Ocean Climate System,* W. K.-M. Lau and D. E. Waliser, Eds., Praxis, 307–360.

Weare, B. C., and J. S. Nasstrom, 1982: Examples of extended empirical orthogonal function analyses. *Mon. Wea. Rev.,* **110,** 481–485.

Webster, P. J., and R. Lukas, 1992: TOGA COARE: The Coupled Ocean–Atmosphere Response Experiment. *Bull. Amer. Meteor. Soc.,* **73,** 1377–1416.

Wheeler, M., and H. Hendon, 2004: An all-season real-time multivariate MJO index: Development of an index for monitoring and prediction. *Mon. Wea. Rev.,* **132,** 1917–1932.

Wu, Z., 2003: A shallow CISK, deep equilibrium mechanism for the interaction between large-scale convection and large-scale circulations in the tropics. *J. Atmos. Sci.,* **60,** 377–392.

Yanai, M., S. Esbensen, and J.-H. Chu, 1973: Determination of bulk properties of tropical cloud clusters from large-scale heat and moisture budgets. *J. Atmos. Sci.,* **30,** 611–627.

Zhang, C., 2005: Madden–Julian Oscillation. *Rev. Geophys.,* **43,** RG2003, doi:10.1029/2004RG000158.

——, and H. H. Hendon, 1997: Propagating and standing components of the intraseasonal oscillation in tropical convection. *J. Atmos. Sci.,* **54,** 741–752.

——, and M. Dong, 2004: Seasonality of the Madden–Julian oscillation. *J. Climate,* **17,** 3169–3180.

——, and S. Hagos, 2009: Bimodal structure and variability of large-scale diabatic heating in the tropics. *J. Atmos. Sci.,* **66,** 3621–3640.

Zhang, G. J., and M. Mu, 2005: Simulation of the Madden–Julian oscillation in the NCAR CCM3 using a revised Zhang–McFarlane convection parameterization scheme. *J. Climate,* **18,** 4046–4064.

——, and X. Song, 2009: Interaction of deep and shallow convection is key to Madden–Julian oscillation simulation. *Geophys. Res. Lett.,* **36,** L09708, doi:10.1029/2009GL037340.